Check for updates

*Advanced Materials Technologies*

ADVANCED MATERIALS TECHNOLOGIES
www.advmattechnol.com

RESEARCH ARTICLE OPEN ACCESS

# Hydro- and Lipophilicity of Molecular-Size-Controlled Hydrogel Drug Carriers

Elisabeth Erbes[1,2] | Naireeta Biswas[1,2] | Calvin J. Gavillet[1,3] | Matthias Schwartzkopf[1] | Krishnayan Basuroy[1] | Qing Chen[1] | Andrei Chumakov[1] | Susann Frenzke[1] | Marc Gensch[1,4] | Korneliya Gordeyeva[5] | Patrycja Kielb[6] | Sonja Kirchner[6] | Volker Körstgens[4] | Peter Müller-Buschbaum[4,7] | Henrike M. Müller-Werkmeister[6] | Jan Rubeck[1] | Sreevidya Thekku Veedu[1] | Jose de Jesus Velazquez-Garcia[1] | Vivian Waclawek[1] | Daniel Söderberg[5] | Stephan V. Roth[1,5] | Simone Techert[1,2]

[1]Deutsches Elektronen-Synchrotron DESY, Hamburg, Germany | [2]Institute for X-ray Physics, Goettingen University, Goettingen, Germany | [3]Department of Mechanics, KTH Royal Institute of Technology, Stockholm, Sweden | [4]TUM School of Natural Sciences, Department of Physics, Technical University Munich, Garching, Germany | [5]Department of Fibre and Polymer Technology, KTH Royal Institute of Technology, Stockholm, Sweden | [6]Institute of Chemistry – Physical Chemistry, Potsdam University, Potsdam, Germany | [7]Heinz Maier-Leibnitz Zentrum (MLZ), Technical University Munich, Garching, Germany

**Correspondence:** Stephan V. Roth (stephan.roth@desy.de; svroth@kth.se) | Simone Techert (simone.techert@desy.de)

**Received:** 11 February 2026 | **Revised:** 5 June 2026 | **Accepted:** 15 July 2026

**Keywords:** drug template | kinetic analysis | lipophilicity | nanolayering | time-resolved x-ray scattering

## ABSTRACT

Nano-sized hydrogel drug carriers with tailored hydro- and lipophilicity are designed and their encapsulation and structure-forming capabilities investigated in real-time. These nano-carriers are built from cellulose and peptide hydrogels in tandem with a nano-stacked interwoven design and alternating hydro- and lipophilicity, thus enabling tuning of the lipophilicity of the carrier mesh for drugs of complementary lipophilicities. This allows for a variety of therapeutic applications, based on the nanoproperties of the hydrogel. Time-resolved and in situ grazing incidence x-ray scattering studies confirm the design and hydro- and lipophilicities of the fiber-hydrogel composite and conclude their ability for carrying drugs of complementary properties site specific. This approach allows for a novel way of understanding the functionality of drug carriers using photon-based approach.

## 1 | Introduction

Not only the worldwide COVID-19 disease as an example of an infectious pandemic, but also the increasing number of other illnesses difficult to treat (like some types of cancer) or individual medical care (like immunization or vaccination) demonstrate the intensive research needed in individual therapeutic treatments or precision medicine [1].

In particular, the experiences with the pandemic showed us that novel pharmaceuticals or those discussed for possible treatments may require new approaches of drug carrier design exploiting also interfaces at the nanoscale. In particular, medications with severe side effects need a highly reliable possibility of nano-dosing to reduce cellular damage caused by drugs. Here, fluid-based technologies allow for the development of materials with nano- or microsized particles with specific properties for biomedical applications. They allow for bottom-up approaches to develop novel approaches for bioimaging, biosensors, tissue engineering, cell encapsulation, drug delivery, separation science, therapeutics, and diagnostics [2]. Bottom-up approaches include additive manufacturing and aerosol-based technologies for facilitating advanced device design, fabrication, and integration on the nano- and microscale [3–5]. Vital for the application is the ability

Elisabeth Erbes and Naireeta Biswas contributed equally to this work.

This is an open access article under the terms of the Creative Commons Attribution License, which permits use, distribution and reproduction in any medium, provided the original work is properly cited.
© 2026 The Author(s). *Advanced Materials Technologies* published by Wiley-VCH GmbH

for time-resolved characterization of the materials' functionality. Microfluidic devices relying on optical methods play an important role here [6]. Organic electronic devices combined with thin film technology allow for studying the interaction of drug compounds with cell membrane lipids in real-time [7].

This requires also to think how pharmaceuticals—the medicine and their carriers—can be characterized very efficiently and quickly in a non-invasive way. Here, we thus introduce a novel non-destructive technology for determining the hydro- and lipophilicity of nano-sized drug carriers with x-rays, based on a kinetic, time-resolved approach.

The nano-carriers as our test benches for the current study ***are built from cellulose nanofibres and peptide hydrogels in tandem*** with a nano-stacked interwoven design and alternating hydro- and lipophilicity, thus enabling tuning of the lipophilicity of the carrier mesh for drugs of complementary lipophilicities. Due to the fabrication type of the composite meshes, pulsed liquid jet and spraying technique (as scalable aerosol technology), their built-up is template-like—and includes, due to the pulsing of the nozzle time, and kinetic information about the fabrication process.

For the current kinetic and time-resolved x-ray approach, we have selected different types of drugs and pharmaceuticals, which have been developed for the treatment of cancer or viral infections. These drugs have been discussed with different proposed inhibition mechanisms, with chemically complementary properties and even controversially debated in the literature [8–17].

To validate our x-ray-based experimental approach, the selection we made is rather based on the drug's chemical properties as "model systems" than based on their supposed antiviral, anti-cancer, or other efficiencies. The results may lead to a generalizable conclusion of determining the properties of nano-dosed drug carriers and their tunability in lipophilicity based on kinetic and time-resolved structural information, which have the potential to be further adapted [18].

The impressive list and number of drugs systematically listed in publicly accessible databases give chemists a rich fund of molecular systems with even opposing chemical (hydrophilic and lipophilic) properties [8–10][1]. While selecting the molecules with opposing chemical properties that also consist of a wide range of drug properties from the molecular databases, we asked the question whether it is possible to develop a nano-based drug carrier matrix that may comprise drugs of opposed hydrophilic and lipophilic or in general, complementary solubility properties. Thus, for this work, we have depicted particular drugs discussed in the context of viral treatments with, for us most importantly, opposing molecular properties, solubility, and interaction with hydrogen networks. Tuning these properties made them ideal candidates for testing whether it is possible to determine their solubility properties and their hydro- and lipophilicity only with our time-resolved and kinetic x-ray studies. Very recently, it has been reported that functionalized nanopolyaniline/fibrin gel composite scaffolds may be used in the treatment of cardiovascular diseases [19]. We also noted that most of the drug molecules picked out in this study imply a high risk of overdose, demanding very precise low-dose control, which added an additional constrain to precise dose's nano-control and x-ray analysis and is targeted with our aerosol-based method.

## 2 | Experiment and Results

The validation samples consist of anti-infectious drugs, singular or in combination, embedded in an interwoven design of nanocellulose fibres and disordered nano-sized peptide hydrogels, fulfilling the desired nano- to micrometer range for potential drug administration [20–23]. These carriers—in particular for these proof-of-concept studies developed—have the potential to overcome some of the current restrictions of nanocellulose-based drug delivery templates [24, 25].

For the proof-of-concept experiment, the samples' structural and morphological integrity under performance conditions. Figure 1A–D introduce into the method of time-resolved and in situ grazing-incidence small-angle x-ray scattering (GISAXS) studies of the fabrication, properties, and functionality of fibre-hydrogel composites as drug carriers. Their template design is schematically shown in Figure 1A. Figure 1B,C presents the time-resolved and in situ GISAXS and in situ grazing incidence medium-angle x-ray scattering (GIMAXS) techniques down to the molecular scale [18–23, 25–27]. The studies, including atomic force microscopy (AFM, Figure 1A) and static and quasi-type in situ Fourier transform infrared spectroscopy (FTIR, later on), allow revealing the different interactions and characterizing the complementary chemical mechanisms of the drug's integration into the fibre-hydrogel composite drug carrier [17, 24]. At this stage, it is important mention to note that the experiments explained in the following section confirm reliable conditions of the fibre and hydrogel composite design for the different active ingredients as well as its suitability for drug storage. Thus, the current study adds another important step into the development of studies on dermatological cellulose and studies on living polypeptides [28–31]. The template of the fibre-hydrogel composite consists of a mixture of hydrophilic carboxy-methylated cellulose fibres (CMC) and peptide hydrogels (P):

CMC is enzymatically active and does not form a hydrogel when dissolved in water, but rather nanofibers, which is confirmed by the GISAXS and GIMAXS analysis. The CMC stacks alter with P hydrogels consisting of variable hydrophilic (Threonin, Serin, Glutamin etc.) and hydrophobic (Glycine-Lysin-Phenylalanine-Glycine) (GLFG)-containing long-chain amino acids, allowing for tuning the hydrophilicity of the P template and therefore allowing for a selective implementation of drugs (for the full peptide sequence, see Supporting Information). CMC and its derivatives also allow for the systematic tuning of hydrogen bonds in the polysaccharide structures [21]. This also enables a local uptake of the active ingredients in a specific chemical environment in CMC [24, 32]. The hydrophobic character of polypeptide chains in P increases with the length of the GLFG peptide chains [22]. The long peptide chains arrange themselves into micellar structures by hydrophilic interactions and hydrophobic collapses—similar to hydrophobic aerogels. Altering the GLFG peptide chains in size and composition allows for a controlled nano-tuning of the hydrophilic and hydrophobic domains.



2365709x, 2026, 20, Downloaded from https://advanced.onlinelibrary.wiley.com/doi/10.1002/admt.71285 by DESY - Zentralbibliothek, Wiley Online Library on [03/11/2026]. See the Terms and Conditions (https://onlinelibrary.wiley.com/terms-and-conditions) on Wiley Online Library for rules of use; OA articles are governed by the applicable Creative Commons License

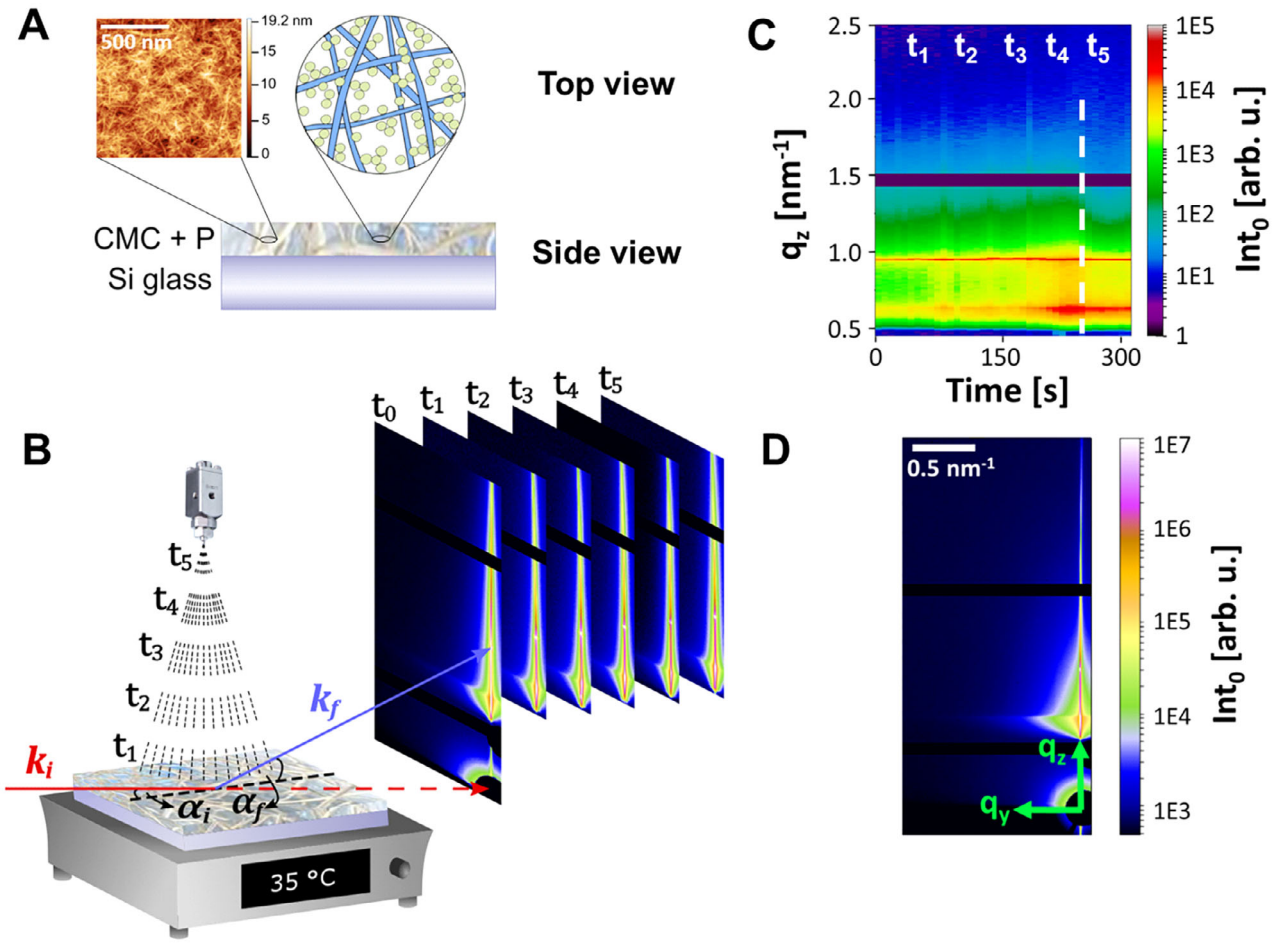



**FIGURE 1** | Time-resolved and in situ GISAXS studies of the fabrication, properties, and functionality of fibre-hydrogel composites as drug carrier. (A) Top view left: AFM image of drug carrier CMC-layers. Top view right: interwoven CMC (blue fibers) and P hydrogel layers (green points), allowing the nano-dosed inclusion of drugs (not shown here) with complementary properties. Side view: mesh carrier design with pre-mixed components. (B) Scheme of the spray set-up used at the P03 beamline at DESY. In situ spray deposition of the drug's solution is performed while analyzing the layering process structures with GISAXS on-the-fly. $t_0$ denotes the time point before spraying drugs and, therefore, the scattering pattern of the pure (CMC + P) drug carrier template without drugs. $t_1$ to $t_5$ are the in situ GISAXS scattering pattern for every spraying cycle at time point $t_{j=1,\ldots,5}$. (C) Every in situ spraying cycle is stroboscopically followed by a fast readout of the detector, which gives additional time information between the spraying cycles. Due to the electronic synchronization, the experiments are highly reproducible (protocol and error bars see SI). The temporal evolution map of the stroboscopically followed density changes along $q_z$ in one in situ experiment of five spraying cycles is shown. The beginning of the figure depicts $t_0$ before the spraying starts ($t_0 = 0$ s), followed by the different spraying cycles. The dashed line depicts the last spraying cycle, and the end of the figure corresponds to the end of the drying process. (D) A typical 2-dimensional GISAXS pattern for the last time point $t_5$.

A typical 2-dimensional GISAXS pattern of a particular spraying time point $t_5$ (loaded with Camostat Mesylate drug) and an overview of the GISAXS curves of selected drugs (Chloroquin Diphosphate (CQD), Camostat Mesylate (CM), Nafamostat Mesylate (NM)), Remdesivir (RD)) embedded in the composite mesh carrier is shown in Figure 2 (resp. Figure 2A,B). Additional GISAXS analysis is found in Figure S1 (see Supplementary Information. In the entire X-ray scattering range, we observe significant intensity modulations when adding the different drugs. The nano- and molecular scale morphology of the carrier nanostructures are determined from the in situ GISAXS ($0.02\ \text{nm}^{-1} < q_y < 0.1\ \text{nm}^{-1}$) and GIMAXS ($0.1\ \text{nm}^{-1} < q_y < 1.2\ \text{nm}^{-1}$) measurements in a two-step analysis:

i. *GISAXS refinement of the fiber-shaped aggregates* ($0.02\ \text{nm}^{-1} < q_y \leq 0.1\ \text{nm}^{-1}$): The horizontal GISAXS cuts within $0.02\ \text{nm}^{-1} < q_y < 0.1\ \text{nm}^{-1}$ (red and blue areas in Figure 2A,B) have been adapted by modelling distributed cylinders/fibers with prolate radii dimensions isotropically [32–35]. The size fitting is limited by the resolution of the GISAXS data for $q_y \leq 0.02\ \text{nm}^{-1}$. The structural parameters obtained from these adjustments have been chosen as limits for the next structural refinement steps.

ii. *GIMAXS fractal refinement* ($0.1\ \text{nm}^{-1} < q_y < 1.2\ \text{nm}^{-1}$): Drug-nanobodies with electron density modulations of molecular orders in the range of $0.1\ \text{nm}^{-1} < q_y < 1.2\ \text{nm}^{-1}$ (green area in Figure 2A,B) have been incorporated into the drug templates in different concentrations. These intensity regions also show drug-dependent intensity modulations in the GIMAXS regime. We have evaluated them using fractal analysis schemes, as explained for Figure 3 following the analysis



2365709x, 2026, 20, Downloaded from https://advanced.onlinelibrary.wiley.com/doi/10.1002/admt.71285 by DESY - Zentralbibliothek, Wiley Online Library on [03/11/2026]. See the Terms and Conditions (https://onlinelibrary.wiley.com/terms-and-conditions) on Wiley Online Library for rules of use; OA articles are governed by the applicable Creative Commons License

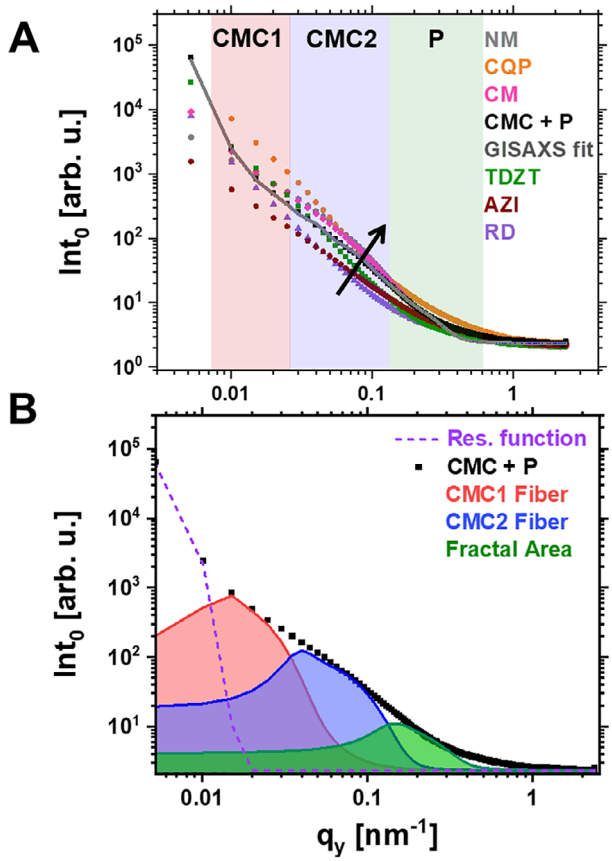



**FIGURE 2** | The different fiber-hydrogel composite drug carrier nano-layers show characteristic domain formations in the different scattering regimes. Domains with larger fiber-shaped CMC aggregates are highlighted as red, and domains with middle-sized CMC units are highlighted as blue areas. The green area of long-chain peptide units P forming fractal networks (green area) are analyzed as follows: (A) Overview of all investigated drugs (for the abbreviation see footnote). Depending on their chemical properties, they embed themselves in the different domain areas relative to the pure fiber-hydrogel composite template (black line). The arrow is added as an eye-guide. Within this scattering regime, drug-only scattering signals do only contribute to the background since not periodically ordered. (B) GISAXS and GIMAXS curves of the pure fiber-hydrogel composite structures without drugs (CMC+P). The green curves indicate 10 nm size structures typical for CMC and starting to overlap with fractal structures formed by small (1–5 nm size) drug molecules. This region needs to be analyzed separately. For clarity of the presentation, we have selected the four most prominent drug candidates in the following section.

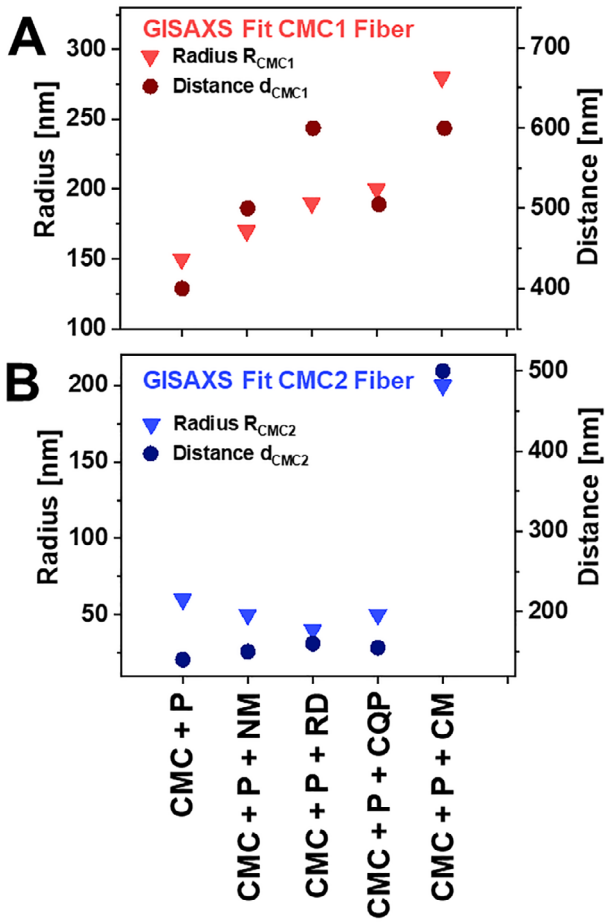



**FIGURE 3** | The different fiber-hydrogel composite drug carrier nano-layers show characteristic domain formations in the different scattering regimes. Domains with larger fiber-shaped CMC aggregates are highlighted as red, and domains with middle-sized CMC units are highlighted as blue areas. The green area of long-chain peptide units P forming fractal networks (green area) are analyzed as follows: Top: refined fiber-shaped aggregation radii $R_{CMC1}$ and inter-fiber distances $d_{CMC1}$. Bottom: refined fiber-shaped aggregation radii $R_{CMC2}$ and $d_{CMC2}$ of the pure fiber-hydrogel composite and the fiber-hydrogel composite loaded with drugs for the red and blue scattering areas (see also Supporting Information). The error bars lay within the size of the plotted data points.

outlined in literature [22, 36–38]. For further information about the analysis, see Figure S2.

The scattering curves analysis according to scheme *(i)* indicates the formation of one large ("CMC1") and one middle-sized ("CMC2") CMC structure with aggregate radii of $R_{CMC1}$ = 150 (±10) nm and $R_{CMC2}$ = 50 (±5) nm as been presented in Figure 3. The same types of fibrillar structures (CMC1 and CMC2) are found when analyzing the GISAXS intensity modulations for pure CMC (see Table S3). When the drugs are embedded in the fiber-hydrogel composite (Figure 3A), the large fiber-shaped CMC aggregates CMC1 swell in size in the drug's order NM, RD, CQP, and CM (Figure 3A; abbreviations [18]). The CMC2 fibers do not change their size (Figure 3B), except for CM loading, which shows additional CMC aggregation behavior. We observe the same trends for the average distances between the fiber-shaped aggregates in the fiber-hydrogel composite, $d_{CMC1}$ and $d_{CMC2}$, and their polydispersity (Table S3).

The big changes in the GISAXS and GIMAXS data of Figure 2A prove a significant embedding of the drugs into the fiber-hydrogel composite and their strong influence on the fiber-hydrogel composite nanomorphology. Detailed analysis in Figure 4A–F shows the quantitative refinement of the (i) GISAXS scattering curves for the drugs CM (Figure 4A), CQP (Figure 4C) and RD (Figure 4E), in comparison to the fractal analysis refined (ii) GIMAXS scattering curves for the drugs CM (Figure 4B), CQP (Figure 4D) and RD (Figure 4F).



2365709x, 2026, 20, Downloaded from https://advanced.onlinelibrary.wiley.com/doi/10.1002/admt.71285 by DESY - Zentralbibliothek, Wiley Online Library on [03/11/2026]. See the Terms and Conditions (https://onlinelibrary.wiley.com/terms-and-conditions) on Wiley Online Library for rules of use; OA articles are governed by the applicable Creative Commons License

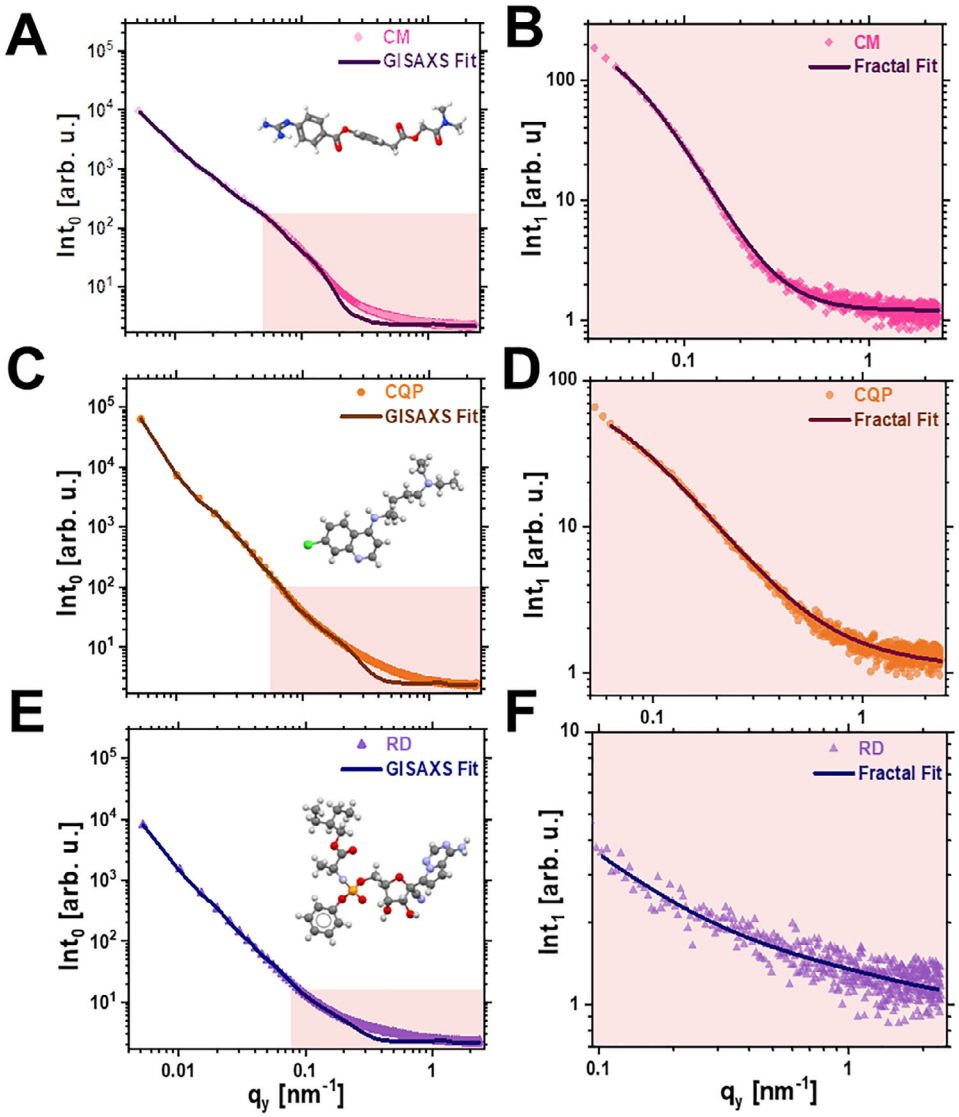



**FIGURE 4** | Representation of the structural adaptation of fiber-hydrogel composite for three representative drugs of this study: Camostat Mesylate (CM), Chloroquine-Phosphate (CQP), and Remdesevir (RD): (A) GISAXS refinement of the CMC network for embedded CM, (B) GIMAXS refinement of the fractal P-network for the embedded CM drug; (C) GISAXS refinement of the CMC network for embedded CQP (it additionally shows a substructure formation at $q_y = 0.01\ nm^{-1}$); (D) GIMAXS refinement of the fractal P-network for the embedded CQP drug; (E) GISAXS refinement of the CMC network for embedded RD; (F) GIMAXS refinement of the fractal P-network for the embedded RM drug. Due to code restrictions, $Int_0$ is the scattering intensity w/o background subtraction, and $Int_1$ is the scattering intensity with subtraction of the GISAXS fit using three structures (see Figure 2A,B). The gas-phase structures acts as references for interpreting the results of the fractal analysis (see also Scheme S5 and description of the calculations).

On one side, we depicted the drugs in such a way that the representative molecular shapes of the drugs are a prolate ellipsoid with two active side groups at both ends for CM, an almost flattened, oblate disk with one active side group terminus for CQP, and a sphere extending with two active side group arms each into all three dimensions for RD.

On the other side, fractal analysis in x-ray scattering, particularly small-angle x-ray scattering, determines the hierarchical structure, aggregation, and surface roughness of nanomaterials by measuring scattered radiation intensity. It analyzes mass/surface fractal dimensions and scaling factors in the power-law scattering region to characterize irregular particles and the porousity of materials, which in particular in this work, connects to the intensity of the hydrogen network formed in the TNP. Continuing the introduced molecular-shape rational, the selected drugs characteristically form tighter or looser hydrogen bonding networks with the fiber-hydrogel composite environment. This depends on the position and type of the chemical side groups relative to the shape of the drug (Figure 5 and Supporting Information, Table S4) and thus according to their (hydrophilicity or) lipophilicity character: Pure P-networks in CMC as reference are characterized by a high nano-porosity, whose electron density structures modulate on the molecular length scale with a peptide radius of $R_P = 0.471 \pm 0.001$ nm, and one order of magnitude larger inter-peptide distances of $5 \pm 0.5$ nm (Table S3, particle center to center distance EIAS).

In Figure 5, the fractal radius $R_P$ defines the smallest self-reproducing structural unit within the network scaled in



2365709x, 2026, 20, Downloaded from https://advanced.onlinelibrary.wiley.com/doi/10.1002/admt.71285 by DESY - Zentralbibliothek, Wiley Online Library on [03/11/2026]. See the Terms and Conditions (https://onlinelibrary.wiley.com/terms-and-conditions) on Wiley Online Library for rules of use; OA articles are governed by the applicable Creative Commons License

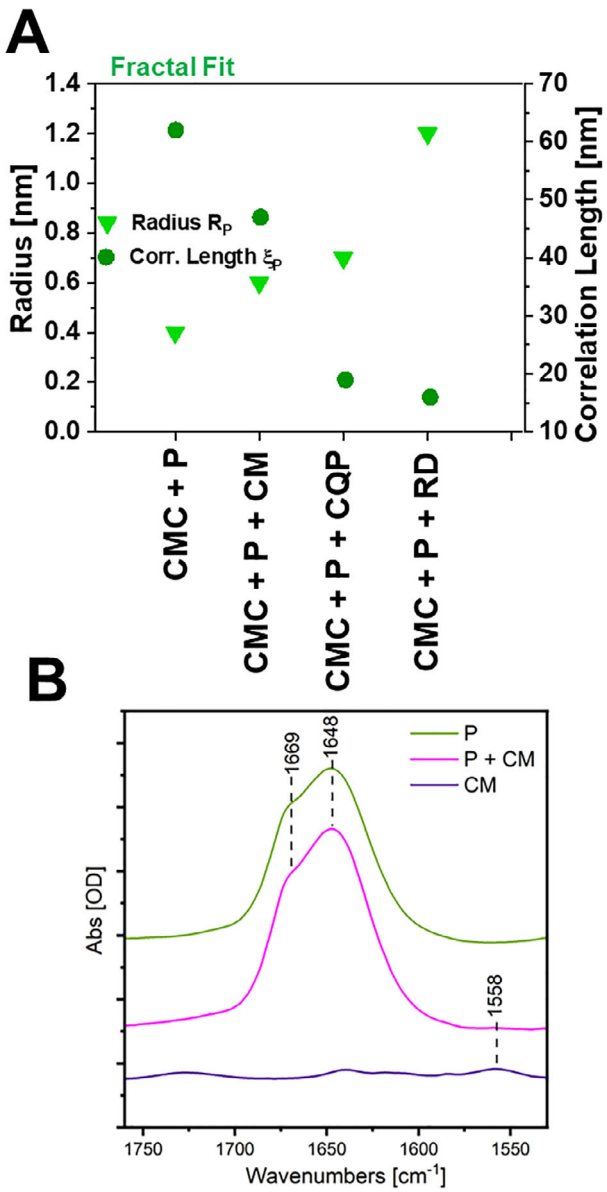



**FIGURE 5** | (A) The fractal radius for the P-network enriched by the drugs increases in the order CMC+P, CMC+P+CM, CMC+P+CQP, CMC+P+RD. The correlation length decreases in the order CMC+P. CMC+RD, CMC+P+CM and CMC+P+CQP. The errors are within the data points. (B) FTIR spectra of pure peptide (P, green), pure CM (CM, violet) and peptide with CM (P + CM, pink) in $D_2O$ confirm a stability of the hydrogen bonding network: A small fraction of ordered beta-turn formation (assigned based on amide I band between 1640–1670 cm$^{-1}$, green) as a secondary structure element is typical for the nanostructure of the P-network within the fiber-hydrogel composite and remains nearly unchanged when CM is added (pink spectra). The FTIR difference spectra are shown in Figure S3.

molecular dimensions. The fractal radius $R_P$ increases with increasing drug's sizes from CM via CQP to RD. Particularly, since CM preferentially adheres to the fibril-shaped CMC aggregates (blue and red area Figure 2A–C), the CMC+P+CM network's fractal radius of 0.45 ± 0.08 nm in Figure 5A (bottom light green, left side and Supporting Information) equalsthe radius of isolated CM molecular units (0.55 nm, determined through quantum chemical simulations (DFT), see SI), which are slightly larger than the smallest P unit (0.47 nm) and can thus be distinguished from them. On the contrary, the correlation length (called $\xi_P$, see Supporting Information) in Figure 5A (right side) refers to the fractal domains' cluster size and shows a reversed order when correlating to the drug's sizes: decreasing from RD to CM to CQP.

We gain additional structural information by adding FTIR studies of the fiber-hydrogel composite components (Figure 5B). $D_2O$ was used as solvent. Figure 3H and Supporting Information, Figure 3 show the FTIR spectra of the amide I and amide II regions corresponding to signals of the peptide bonds (bands between 1640–1670 cm$^{-1}$ and 1420–1460 cm$^{-1}$ of the pure P-network (green) and loaded with CM (pink). The amide I band, centered at 1640–1665 cm$^{-1}$ exhibits a clear signature for beta-sheets and -turns (shoulder at 1669 cm$^{-1}$) in combination with the presence of random structures (peak at 1648 cm$^{-1}$) [39]. When loaded with a drug (equal preparation conditions as in the GISAXS/GIMAXS studies), the amide I and amide II band with their typical side shoulders remain nearly unaffected suggesting that the beta-sheet structures remain unaltered during drug loading of the fiber-hydrogel composite, corroborating the encapsulation of the drug.

## 3 | Interpretation and Discussion

What do these observations now imply concerning the drug's pharmaceutical properties such as their *lipophilicity or hydrophilicity?* For obtaining a more detailed understanding of the drugs solubility in the fiber-hydrogel composite, we correlate our structural results with the so-called *lipophilicity or hydrophilicity* parameters of the drugs: According to their definition [8, 9, 40–48], lipophilicity or the lipophilicity parameters of drugs are correlated to their solvation entropies driving hydrophilic and hydrophobic effects of drugs when dissolved or embedded into pharmaceutical relevant matrices like, in our case, the studied fiber-hydrogel composites.

As already mentioned in the explanation of Figures 2–5, the majority of known drugs contain ionizable groups which are charged at physiological pH. For considering the pH-corrected properties, high-performance liquid chromatography (HPLC)-based $\log D_{7.4}$ values had been introduced. $\log D_{7.4}$ scales the lipophilicity to octanol/water (pH 7.4) standards and is reported in various data banks [43]. Negative $\log D_{7.4}$ values ($\log D_{7.4} < 0$) indicate high hydrophilicity, and positive $\log D_{7.4}$ values ($\log D_{7.4} > 0$) indicate low hydrophilicity and high lipophilicity. Another measure for the hydro- or lipophilicity of the drugs is the protein binding value in % [44]. Values < 50% indicate high hydrophilicity, values > 50% high lipophilicity of the drugs.

In Figure 6 we correlated the derived structural parameters of the drug-loaded fiber-hydrogel composites, their nanocellulose and peptide radii of gyration ($R_{CMC1}$, $R_{CMC2}$, $R_P$) with the pharmaceutical solubility parameters $\log D_{7.4}$ value, the protein binding value, and their general lipo- and hydrophilcities.

These results allow for a concise picture of the various static hierarchies of the fiber-hydrogel composite structures and how they are changed when loaded with drugs of opposing hydro- to



2365709x, 2026, 20, Downloaded from https://advanced.onlinelibrary.wiley.com/doi/10.1002/admt.71285 by DESY - Zentralbibliothek, Wiley Online Library on [03/11/2026]. See the Terms and Conditions (https://onlinelibrary.wiley.com/terms-and-conditions) on Wiley Online Library for rules of use; OA articles are governed by the applicable Creative Commons License

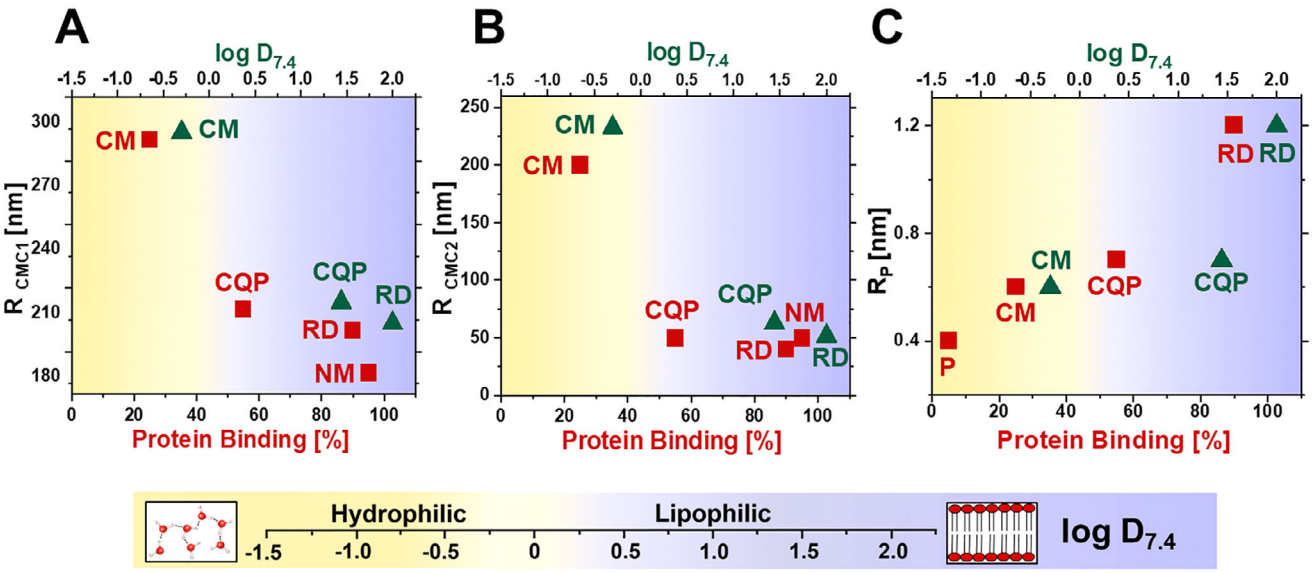



**FIGURE 6** | Correlation between the structural analysis of the drug-loaded fiber-hydrogel composite and the lipophilicity parameter of the drugs. Top: Dependencies on the $logD_{7.4}$ value; Bottom: dependencies on the protein binding [%] values, both tabulated solubility characteristics of pharmaceuticals. (A) CMC1 large fiber $R_{CMC1}$ of CM, CQP, RD and NM. (B) medium-sized fiber $R_{CMC2}$ (50 nm) of CM, CQP, RD and other studied drugs and (C) fractal radii of the CMC and P-domains ($R_P$) of the fiber-hydrogel composite of the different drugs as a function of the lipophilicity parameters $logD_{7.4}$ (top) and %-protein binding values (bottom).

lipophilicity in a static description (Figure 2C top, Tables S3 and S4, to Figure 5). The larger radii of gyration of the CMC1 fiber-like subphase (aggregates), $R_{CMC1,}$ increase characteristically without and with peptide and drug loading from $R_{CMC1}$(CMC+P) = 150 ± 12 nm to $R_{CMC1}$(CMC+P+RD) = 190 ± 20 nm, to $R_{CMC1}$(MC+P+CQP) = 200 ± 15 nm, and to $R_{CMC1}$(CMC+P+CM) = 280 ± 25 nm.

Quantitative values for the lipo-/hydrophilicity of the drugs are given in terms of $logD_{7.4}$ values. As the drugs become more lipophilic, the $logD_{7.4}$ values increase from negative to positive values, resulting in tighter packing of CMC1- fiber-hydrogel composite and a decrease in $R_{CMC1}$ as a function of $logD_{7.4}$ or protein binding (Figure 6A). The system segregates during fiber-hydrogel composite formation, leading to a strong separation of the CMC and P domains, allowing the structures to organize themselves more densely. CM exhibits the highest hydrophilicity among the drugs studied and causes the most significant swelling of the CMC1 network. This is evidenced by the substantial increase in $R_{CMC1}$ from 190 ± 12 nm to 280 ± 25 nm. In contrast, CQP and RD, which are relatively lipophilic, show less interaction with the CMC network, resulting in $R_{CMC1}$ values of around 190–200 nm.

$R_{CMC2}$ is an intermediate structure of a CMC phase consisting of smaller structures. The size of $R_{CMC2}$ for CMC, CMC+P, CMC+P+RD, and CMC+P+CQP ranges from 40 to 60 nm (Figure 2C; Table S3, Figure 6B). For CMC+P+CM, however, $R_{CMC2}$ has a value of 200 ± 18 nm, indicating a significant swelling characteristic for the CMC domain due to specific interactions with CM. The observed slight changes in $R_{CMC2}$ are consistent with the results obtained from $R_{CMC1}$, as shown in Figure 3A,B. The decrease if $R_{CMC2}$ correlates directly with the increase in log $D_{7.4}$ for the screened drugs. The distance between the centers of particles CMC1 and CMC2 decreases as the fiber wall-to-wall distance decreases. The third structure, which yields intensity in the green region of Figure 2B, ranges between 10 and 15 nm for CMC, CMC+P, CMC+P+RD, CMC+P+CQP (Table S3), while being 20 ± 3 nm for CMC+P+CM.

An inverse dependence of the smallest refined radii of gyration $R_P$ is observed when comparing the classical phase shape evaluation with the fractal analysis in Figures 4 and 5. These radii describe the fractal network of the peptide mesh/subphase. They also depend on the lipophilicity parameter $logD_{7.4}$, but inversely to $R_{CMC1}$ or $R_{CMC2}$. Upon loading with drugs, the P-mesh undergoes a significant swelling from $R_P$(CMC+P) = 0.471 ± 0.001 nm: $R_P$ gradually increases from $R_P$(CMC+P) = 0.471 ± 0.001 nm to (CMC+P+CM) = 0.58 ± 0.01 nm to $R_P$(CMC+P+CQP) = 0.74 ± 0.05 nm to $R_P$(CMC+P+RD) = 1.22 ± 0.06 nm as $logD_{7.4}$ and the lipophilicity increases (Table S4; Figure 6C). Compared to the unloaded fiber-hydrogel composite CMC+P, the lipophilic P-phase of the fiber-hydrogel composite slightly de-packs and structurally disorders, when loaded with more hydrophilic CM, yielding a very small $R_P$ increase (Figure 6C). Dissolving hydrophilic CM in the hydrophobic P-phase does not lead to molecular solvation stabilization but it results in better solvation into the hydrophilic CMC1 and CMC2 subphases (increase of their radii of gyration, Figure 6A,B), with a larger segregation of the CMC from the P phases: the hydrophilicity of the drug embedded significantly affects the extent of segregation of the subphases during fiber-hydrogel composite formation.

Figure 6 clearly demonstrates that CM is the most hydrophilic drug among those studied. As a result, it causes the most significant swelling of the hydrophilic CMC phases, as evidenced by the increase in $R_{CMC1}$ and $R_{CMC2}$. The addition of drugs to the fractal template leads to an increased $R_{CMC1}$, which in turn causes a decrease in fiber wall-to-wall distances and a reduction in correlation lengths $\xi_P$ between two CMC fibers. Table S3,



2365709x, 2026, 20, Downloaded from https://advanced.onlinelibrary.wiley.com/doi/10.1002/admt.71285 by DESY - Zentralbibliothek, Wiley Online Library on [03/11/2026]. See the Terms and Conditions (https://onlinelibrary.wiley.com/terms-and-conditions) on Wiley Online Library for rules of use; OA articles are governed by the applicable Creative Commons License

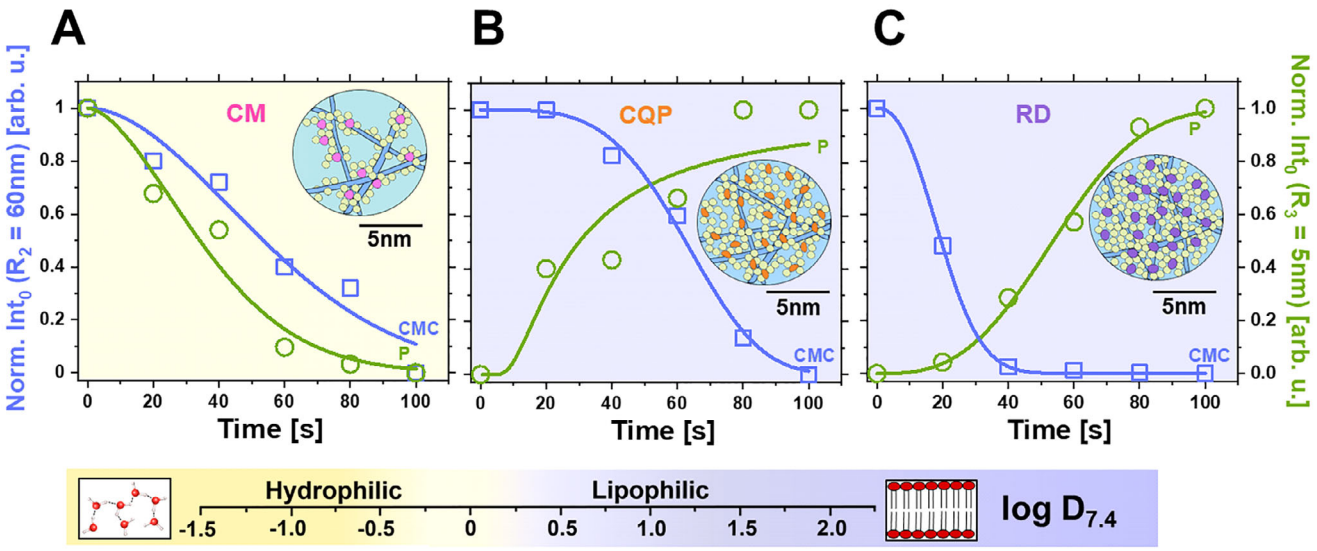



**FIGURE 7** | In situ kinetic and structural analysis of the drug embedding during the spray production of the fiber-hydrogel composite. All three fiber-hydrogel composite formations are kinetically driven. The insets present the final fiber-hydrogel composite-drug structures and morphologies after the last spraying cycle with CMC structures in blue, smaller green dots for peptides, and larger pink dots for the drugs. (A) For CM, a decomposition of the 50 nm-middle-sized, fiber-shaped CMC aggregates (blue curve) and fractal P-network (green curve intensities) is seen: Both curves decrease. This implies a formation of specific P-drug fractal substructures around swollen fiber-shaped CMC aggregates. (B) For CQP, a dissolution of the 50 nm-middle-sized CMC fibers is seen (blue curve decreases). Formation of aggregates within the P-network between the long fiber-shaped CMC aggregates is observed (green curve increases). (C) For RD, a faster dissolution of the middle-sized, 50 nm fiber-shaped CMC aggregates (blue curve decreases) under comparable concentration conditions is observed. The formation of the CMC-P-network with RD embedded in the fractal P-network and between the long fiber-shaped CMC aggregates is delayed and kinetically hindered (green curve increase). The variation of the CMC and P nanoparticle aggregation properties has been presented as needles and dots in the round insets of this Figure and reflected in the variations of the poydispersity values of Table S3.

demonstrates that $\xi_P$ decreases in the order CQP, CM, RD. This indicates that the degree of cooperative structural organization within the fiber-hydrogel composite becomes more pronounced as the drugs become more hydrophilic.

Coming to the area of fractal interpretation (GIMAXS area), lipophilic drugs, like CQP and RD, enter the peptide network instead of the porous cellulose network: as the CMC1 and CMC2 radii of gyration decreases with loading of the fiber-hydrogel composite with CQP and RD, the radii of gyration of P-mesh ($R_P$) increase due to a preferred solvation within the lipophilic P-phase.

Concerning dynamic studies, we performed additional in situ real-time GISAXS and GIMAXS studies of the fiber-hydrogel composite formation. Figure 7A–C (and corresponding Figure S4) confirm drastic differences in the kinetics of the fiber-hydrogel composite production for the various drugs—in particular when reaching the drug's concentration saturation conditions at the end of the spraying process. The separate time points are defined by a spraying and drying cycle of one fiber-hydrogel composite layer (and between two spray pulses). For the analysis, we focus on the normalized intensity of CMC2 and P region in Figure 2A,B (see also Figures S3 and S4) in order to differentiate between the dynamics of formation and restructuring of the cellulose and peptide domains.

In a wider sense, hydrophilicity can also be determined by the geometrical wetting properties of a liquid drop on a defined surface (for definitions, see Supporting Information). With our time-resolved x-ray scattering studies, as expressed in Figure 6, we make use of the correlation between the log $D_{7.4}$ value and hydrophilicity properties and its geometrical pendant, by studying the nanoscale properties and nanoscale structural evolution of our drug-target entities during the spraying, droplet creation, and finally film formation of the drug:CMC:peptide units. With the structural methods, we determine the structural features underlying the growing process of the template.

The lipophilicity of the drug has a significant impact on the formation of fiber-hydrogel composite. However, the kinetic response function of the fractal network is more complex during fiber-hydrogel composite formation. The temporal analysis of the drug's interaction with fiber-hydrogel composites, as depicted by the blue lines in Figure 7 (more precise in Figure 7A–C), were obtained from the normalized intensities in the blue areas of Figure 2 (and Figure 4 resp. Figure S3). The in situ experiment primarily monitors time-dependent changes in the middle-sized structural CMC2-fiber network. The green line depicts the time evolution of the normalized intensities derived from the green area, which belongs to the fractally organized P-network of the fiber-hydrogel composite. The original CMC2-fiber network partially disappears in all three systems as the blue curves decrease in intensity.

The rate constants are globally determined by the fiber-hydrogel composite layer-to-layer growth, as shown in Figure 7 and Figure S4. The error bar of the time traces only, including the



2365709x, 2026, 20, Downloaded from https://advanced.onlinelibrary.wiley.com/doi/10.1002/admt.71285 by DESY - Zentralbibliothek, Wiley Online Library on [03/11/2026]. See the Terms and Conditions (https://onlinelibrary.wiley.com/terms-and-conditions) on Wiley Online Library for rules of use; OA articles are governed by the applicable Creative Commons License

experimental jitter, is smaller than 500 msec. The error of the determined intensities lays within the symbol size. Further statistical values are described in the Supporting Information. For the sample and data collection averaged kinetics, the half-time rate constants $k_{1/2}$ for the different systems, CMC+P+CM, CMC+P+CQP and CMC+P+RD are in general of the same order of magnitude and depend on the spraying doses/drying cycles. In concrete terms we find for the kinetics of the fiber-hydrogel composite formation with CM $\tau_{1/2}$(CMC+P+CM, P) = 35 ± 2 s, $\tau_{1/2}$(CMC+P+CM, CMC) = 55 ± 5 s, for the ones with CQP $\tau_{1/2}$(CMC+P+CQP, P) = 30 ± 2 s, $\tau_{1/2}$ (CMC+P+CQP, CMC) = 62 ± 5 s, and a rate reversing and fastening of the process for RD with $\tau_{1/2}$(CMC+P+RD, P) = 55 ± 5 s and $\tau_{1/2}$ (CMC+P+RD, CMC) = 20 ± 2 s.

Figure 7 clearly outlines the differences in the slope of the fiber-hydrogel composite growing rate constants between CM, CQP, and RD. It is observed that the hydrophilic CM system exhibits opposite kinetic behavior compared to the more lipophilic CQP and RD systems. The observed kinetic behavior in Figure 7A for CM can be attributed to the structural decomposition of the original middle-sized, fiber-shaped CMC aggregates (blue curve decreases, left scale) and fractal P-network aggregates (green curve intensities decrease, right scale). The segregation process results in the formation of slightly disordered but specific CM-drug fractal-P-substructures around swollen fiber-shaped CMC aggregates, as demonstrated in Figures 2–6.

The FTIR results confirm that the $\beta$-sheet type of the P-fiber-hydrogel composite structure persists during this reorganization in the nanodomains. Additionally, more lipophilic CQP still effectively dissolves the middle-sized CMC fibers (as evidenced by the blue curve decrease), but also forms ordered substructures and aggregates within the lipophilic P-network between the long fiber-shaped CMC aggregates (as evidenced by the green curve increase). These findings demonstrate the efficacy of CQP in restructuring the P- and the CMC-phases (aggregates). RD exhibits a similar kinetic behaviour to CQP (Figure 7C). However, under comparable conditions, RD dissolves the middle-sized fiber-shaped CMC aggregates faster and more effectively than CQP. The formation of the CMC-P-network, with RD embedded in the fractal P-network and between the long fiber-shaped CMC aggregates, is delayed and kinetically hindered (as shown by the delayed increase of the green curve in Figure 7C).

The original CMC2-fibril network partially disappears in all three systems as the blue curves decrease in intensity (Figure S3). However, the different drugs partially exhibit self-amplifying and autocatalytic reactions of increasing intensity, with comparable concentrations and slope characteristics but different time constants:

- The disassembly of the hydrophilic CMC2 fiber network in the hydrophilic CM's case results in the thinning out of the fractal hydrophobic P-network at comparable kinetic rates to the dilution of fiber-shaped CMC2-aggregates (as shown in Figure 7A). It is worth noting that the disassembly of the hydrophobic P-network is autocatalytically accelerated compared to the ones of the CMC phases. Out of all the drugs, the most significant correlation length is demonstrated for CM (Figure 4A). It is observed that CM forms clusters within the dissolved P- and CMC-mesh. These clusters are likely to accumulate on the surface of the large fiber-shaped structures, as suggested by the radius and distance increase in Figure 3A, for CM. The mechanism of this process is illustrated in the inset of Figure 7A. The relocation of the P-assembled structures to other areas within the fiber-hydrogel composite implies that the disordered arms of the P-mesh loosen their network between the fibers and compactly arrange themselves with the drugs around the fibers. These findings demonstrate a clear understanding of the incorporation of CM into the fiber-hydrogel composite.
- More lipophilic CQP and RD dissolve CMC2-aggregates of fiber structures in classical first-order reactions, with RD being faster than CQP. The kinetic analysis clearly demonstrates that CQP autocatalytically enriches the interstitial P-mesh, thereby accelerating the increase in fiber-hydrogel composite structural compactness, outpacing the dissolution of the fiber-shaped CMC2 aggregates (as shown in Figure 7B, inset). Both prefer solvation within the P-mesh.
- Lipophilic RD enhances the P-phase formation, as demonstrated by the intensified green curve in Figure 7C. The time constant of this process follows a classical first-order kinetic law, similar to the disassembly of CMC2-aggregates, rather than an autocatalytic kinetics.

The CMC2 aggregate domains for all three drugs consist of two sub-phases: one forming larger or more swollen CMC fibers (Figure 3A/Figure 4), and one with much smaller fiber aggregation radii, slightly larger than the typical fractal network dimensions (Tables S3 and S4). Our in situ and real-time measurements of fiber-hydrogel composite production thus demonstrate two important aspects for storing these drugs/drug models with opposing lipophilicity. As to Figure 6, the nanostructure of the drug matrix is crucial in kinetically controlled drug delivery, in particular for low-dosage treatments. Incorporating hydrophilic (cellulose) and hydrophobic (peptides) nano-units can create optimized direct next-neighbor conditions for different drugs. Regulating the local concentration of matrix/host formation during fiber-hydrogel composite fabrication can be achieved by controlling phase transformations and segregation when drugs are embedded. Among the studied drug systems, it is evident that CM undergoes the most significant structural rearrangement when embedded into the fiber-hydrogel composite. This is because of the structural response function of CM adapting to its compartment environment and adjusts the hydrogen network to backbone structures such as the peptides. The drug/host system of CM embedded in our fiber-hydrogel composite (i.e., CMC + P) is highly promising due to the structure of CM and the flexibility of the peptide network.

## 4 | Conclusions

In summary, the autocatalytic embedding of CM in fiber-hydrogel composite is unequivocally supported by CM's specific chemical interactions with the P-network/mesh. These interactions lead to a preferential restructuring around the fibril-shaped CMC aggregates. Out of all the drugs and model drugs studied, CM displays the most exceptional matrix solubility behavior due to its remarkably high degree of hydrophilicity. CQP exhibits



2365709x, 2026, 20, Downloaded from https://advanced.onlinelibrary.wiley.com/doi/10.1002/admt.71285 by DESY - Zentralbibliothek, Wiley Online Library on [03/11/2026]. See the Terms and Conditions (https://onlinelibrary.wiley.com/terms-and-conditions) on Wiley Online Library for rules of use; OA articles are governed by the applicable Creative Commons License

intensive chemical interactions with the P-network between the fiber-shaped CMC-aggregates. RD selectively enriches within the hydrophobic P-network, intermixing with the CMC-phases, inducing structural disorder properties in the CMC network during embedding. CM exhibits hydrophilic properties, CQP is weakly lipophilic, while RD is highly lipophilic.

Structurally, the hydrophilic interactions of CM lead to two autocatalytically enhanced reorganizations of both the fractal P and the middle-sized CMC2 nano-networks from their original shapes toward a higher-dimensional network. During dissolving CM in the CMC network, the process of diluting the CMC2 nano-cylinders causes a significant swelling in size of the larger CMC1 nano-cylinders. We interpret this as a reformation of the fiber-hydrogel composite units around the CMC1 nano-cylinder network, at the expense of the CMC2 and in particular P-units, in favor of the CMC1 units.

In contrast, the highly lipophilic RD strongly dilutes within the hydrophobic P-network, forming solvated structures and effectively increasing its fractal radius due to the enlargement of the structural P-solvation shell. The slightly higher density of the CMC-network is also a direct result of this. The CMC2 nano-cylinders undergo partial dissolution, while the CMC1 nano-cylinders experience slight swelling. It is important to note that CQP, which has weak lipophilicity, shows a similar trend though more pronounced.

The fiber-hydrogel composite developed within this framework is an ideal carrier platform that can be customized for all types of drugs, whether hydrophilic or lipophilic. This is due to the fiber-hydrogel composite's ability to individually reorganize around the drug, being hydro- or lipophilic. This results in a drug-specific stabilization of the drug's solvation by structurally patterning the overall hydro- or lipophilicity of the fiber-hydrogel composite. Predictively, hydrophilic drugs will autocatalytically reshape the fiber-hydrogel composite toward a reorganization stabilizing the drug's solvation by remaining fiber-hydrogel composite's overall lipophilicity. This makes the fiber-hydrogel composite an excellent carrier material for all types of drugs—hydrophilic as well as lipophilic ones. The fiber-hydrogel composite has the potential to administer drugs at controlled low doses and in a variable manner to reduce severe side effects. The novel non-destructive and non-invasive concept for determining the hydro- and lipophilicity of with dynamic x-ray studies within the nanocellulose/fiber network being characteristic for cellulose-based paper enables the development of drug carriers as "Therapeutic Nanopaper".

Drug release studies will, however, be the topic of future pharmaceutical studies as well as extending our studies to other drug candidates and types. Emphasizing the method and strategy development in this work, for pharmaceutical research in the field of cancer and related areas, we propose a strategy that still needs to be refined for certain vectors.

### Author Contributions

The therapeutic nano-paper and its chemical subunits have been designed by: E.E., S.F., C.B., Q.C., K.G., D.S., S.R. (CMC); N.B., K.B., S.T. (peptide); S.T.V., J.V.G., S.F. (drug inclusion). In situ thin films have been grown by E.E., M.S., C.G. and Q.C. Time-resolved and in situ GISAXS has been collected by N.B., E.E., M.S., J.R., M.G., C.G., V.W., A.C., Q.C., S.R. and S.T. under special pandemic operation constrains. C.G., E.E. and D.S. added A.F.M. studies. The chi2 analysis has been performed by E.E. and N.B., with contributions (MS) and helpful discussions from M.S., V.K. and P.M.B.; E.E., N.B. and S.T. integrated additionally the SASView analysis (also in the Supporting Information). P.K., S.K. and H.M.W. contribute with the in situ FTIR studies. N.B., E.E., S.V.R and S.T. wrote the manuscript.


### Acknowledgements

The project is supported by HGF-Recruitment-DESY, HGF-InnovPool-FISCOV, HGF-InnovPool-FISVIR and HGF-POF-IV-RT3. S.T. and H.W.M. are in particular grateful to financial support of the ESP program of the CMWS/DESY. S.R. and S.T. acknowledge DESY and DESY-FS for beamtime granting and special access during a CORONA-call of PETRA III. C.B. and S.R. acknowledge funding from DESY strategic fund (DSF) "Investigation of processes for spraying and spray-coating of hybrid cellulose-based nanostructures". S.T. acknowledges CRC1633 – Pushing Electrons with Protons (DFG/510228793) and Exc-3120 BlueMAT—Water-driven Materials (DFG/533771286). This work benefited from the use of the SasView application, originally developed under NSF award DMR-0520547. SasView contains code developed with funding from the European Union's Horizon 2020 research and innovation program under the SINE2020 project, grant agreement no. 654000.


### Conflicts of Interest

The authors declare no conflicts of interest.

### Data Availability Statement

Data about the experimental conditions, codes, and materials are available in the main text or SI. The data that support the findings of this study are available from the corresponding author upon reasonable request.

### ENDNOTE

[1] In alphabetical order, the named drugs range from (serine) protease inhibitors as Camostat Mesylate (CM) or Nafamostat Mesylate (NM) (7-10) through (non-specific) inflammatory TLR7-9 inhibitors, as Hydroxychloroquine Sulfate, ATM activators, such as Chloroquine Diphosphate (CQP) (11,12), antiviral RNA-blocking broad-spectrum agents, as Remdesivir (RD) (11), HMG-CoA reductase inhibitors, as the statin Pitavastatin Calcium (13) to non-ATP competitive serine kinase inhibitors-8 (TDZD) (14), and their combination with the antibiotics Azetomycin (AZI)

### References


1. F. S. Collins and H. Varmus, "A New Initiative on Precision Medicine," *New England Journal of Medicine* 372, no. 9 (2015): 793–795.

2. X. Luo, P. Su, W. Zhang, and C. L. Raston, "Microfluidic Devices in Fabricating Nano or Micromaterials for Biomedical Applications," *Advanced Materials Technologies* 4, no. 12 (2019): 1900488.

3. W. Yang, S. Cai, Y. Chen, et al., "Modular and Customized Fabrication of 3D Functional Microgels for Bottom-Up Tissue Engineering and Drug Screening," *Advanced Materials Technologies* 5, no. 5 (2020): 1900847.

4. J. Choi, J. K. Sahoo, O. Hasturk, T. Falcucci, Y. Yao, and D. L. Kaplan, "Instantaneous Formation of Silk Protein Aerosols and Fibers With a Portable Spray Device Under Ambient Conditions," *Advanced Materials Technologies* 8, no. 7 (2023): 2201392.

5. R. Nithyananda, A. Ramirez, P. Verding, et al., "Deposition of Ultra-Thin Coatings by a Nature-Inspired Spray-on-Screen technology," *Communications Engineering* 2 (2023): 42.

6. O. M. Rahman, S. Lan, and D. K. Hwang, "Architecture of an All-In-One Microfluidic Platform for Accelerated Cancer Seeding, Enhanced





2365709x, 2026, 20, Downloaded from https://advanced.onlinelibrary.wiley.com/doi/10.1002/admt.71285 by DESY - Zentralbibliothek, Wiley Online Library on [03/11/2026]. See the Terms and Conditions (https://onlinelibrary.wiley.com/terms-and-conditions) on Wiley Online Library for rules of use; OA articles are governed by the applicable Creative Commons License

Spheroid Formation, and Dynamic Drug Screening Trials," *Advanced Materials Technologies* 11, no. 7 (2025): e01747.

7. P. Cavassin, A.-M. Pappa, C. Pitsalidis, et al., "Organic Transistors Incorporating Lipid Monolayers for Drug Interaction Studies," *Advanced Materials Technologies* 5, no. 3 (2020): 1900680.

8. V. Pliška, B. Testa, and H. Waterbeemd, *Lipophilicity in Drug Action and Toxicology* (VCH Verlagsgesellschaft mbH, 1996).

9. National Center for Biotechnology Information 2024. *Partition Coefficient (logD7.4)* from https://pubchem.ncbi.nlm.nih.gov/bioassay/19424.

10. L. Felton, *Remington Essentials of Pharmaceutics*, 21th Edition (Pharmceuticals Press, 2023).

11. M. Hoffmann, H. Kleine-Weber, S. Schroeder, et al., "SARS-CoV-2 Cell Entry Depends on ACE2 and TMPRSS2 and is Blocked by a Clinically Proven Protease Inhibitor," *Cell* 181, no. 2 (2020): 271–280.e8.

12. Y. Uno, "Camostat Mesilate Therapy for COVID-19," *Internal and Emergency Medicine* 15 (2020): 1577–1578.

13. M. Yamamoto, S. Matsuyama, X. Li, et al., "Identification of Nafamostat as a Potent Inhibitor of Middle East Respiratory Syndrome Coronavirus S Protein-Mediated Membrane Fusion Using the Split-Protein-Based Cell-Cell Fusion Assay," *Antimicrobial Agents and Chemotherapy* 60 (2016): 6532–6539.

14. M. Hoffmann, S. Schroeder, H. Kleine-Weber, M. A. Müller, C. Drosten, and S. Pöhlmann, "Nafamostat Mesylate Blocks Activation of SARS-CoV-2: New Treatment Option for COVID-19," *Antimicrobial Agents and Chemotherapy* 64, no. 6 (2020): e00754.

15. M. Wang, R. Cao, I. Zhang, et al., "Remdesivir and Chloroquine Effectively Inhibit the Recently Emerged Novel Coronavirus (2019-nCoV) In Vitro," *Cell Research* 30 (2020): 269–271.

16. M. Hoffmann, K. Mösbauer, H. Hofmann-Winkler, et al., "Chloroquine Does Not Inhibit Infection of Human Lung Cells With SARS-CoV-2," *Nature* 585 (2020): 588–590.

17. F. J. Frost, H. Petersen, K. Tollestrup, and B. Skipper, "Influenza and COPD Mortality Protection as Pleiotropic, Dose-Dependent Effects of Statins," *Chest* 131, no. 4 (2007): 1006–1012.

18. J. Hettinga and R. Carlisle, "Vaccination Into the Dermal Compartment: Techniques, Challenges, and Prospects," *Vaccines* 8, no. 3 (2020): 534.

19. D. Zhang, N. Wang, Q. Liu, et al., "Functionalized Nanopolyaniline/Fibrin Gel Composite Scaffolds: Implications for the Treatment of Cardiovascular Disease," *ACS Applied Nano Materials* 6, no. 23 (2023): 21503–21513.

20. K. Håkansson, A. Fall, F. Lundell, et al., "Hydrodynamic Alignment and Assembly of Nanofibrils Resulting in Strong Cellulose Filaments," *Nature Communications* 5 (2014): 4018.

21. C. J. Brett, N. Mittal, W. Ohm, et al., "Water-Induced Structural Rearrangements on the Nanoscale in Ultrathin Nanocellulose Films," *Macromolecules* 52 (2019): 4721–4728.

22. M. Petri, A. Menzel, O. Bunk, G. Busse, and S. Techert, "Concentration Effects on the Dynamics of Liquid Crystalline Self-Assembly: Time-Resolved X-ray Scattering Studies," *The Journal of Physical Chemistry A* 115 (2011): 2176–2183.

23. M. Petri, S. Frey, A. Menzel, D. Görlich, and S. Techert, "Structural Characterization of Nanoscale Meshworks Within a Nucleoporin FG Hydrogel," *Biomacromolecules* 13, no. 6 (2012): 1882–1889.

24. T. V. Patil, D. K. Patel, S. Deb Dutta, K. Ganguly, T. Subhra Santra, and K. Lim, "Nanocellulose, a Versatile Platform: From the Delivery of Active Molecules to Tissue Engineering Applications," *Bioactive Materials* 9 (2022): 566–589.

25. T. Abitbol, A. Rivkin, Y. Cao, et al., "Nanocellulose, a Tiny Fiber With Huge Applications," *Current Opinion in Biotechnology* 39 (2016): 76–88.

26. S. Bari, R. Boll, and K. Idzik, *Fundamentals and Application of Free-Electron Lasers*, ed. U. Bergmann, V. Yachandra, and J. Yano, (Royal Chemical Society, 2017), 301.

27. J. Velazquez-Garcia, K. Basuroy, D. Storozhuk, et al., "Short- vs. Long-range elastic distortion: Structural dynamics of a [2 × 2] Tetrairon( ii ) Spin Crossover Grid Complex Observed by Time-Resolved X-Ray Crystallography," *Dalton Transactions* 51, no. 46 (2022): 17558–17566.

28. F. Thorimbert, A. Brachfeld, M. Odziomek, et al., "Microfabrication Through Self-Ordering of Cracks: Mechanism, Upscaling and Application for Transparent Electrodes," *Advanced Materials Technologies* 9, no. 16 (2024): 2400353.

29. M. Wang, L. Xu, H. Hu, et al., "Radiation Synthesis of PVP/CMC Hydrogels as Wound Dressing," *Nuclear Instruments and Methods in Physics Research Section B: Beam Interactions with Materials and Atoms* 265, no. 1 (2007): 385–389.

30. P. Liu, M. Zhai, L. Jiuqiang, P. Peng, and W. Jilan, "Radiation Preparation and Swelling Behavior of Sodium Carboxymethyl Cellulose Hydrogels," *Radiation Physics and Chemistry* 63, no. 3–6 (2002): 525–528.

31. T. Aliferis, H. Iatrou, and N. Hadjichristidis, "Living Polypeptides," *Biomacromolecules* 5, no. 5 (2004): 1653–1656.

32. G. Benecke, W. Wagermaier, C. Li, et al., "A Customizable Software for Fast Reduction and Analysis of Large X-Ray Scattering Data Sets: Applications of the New DPDAK Package to Small-Angle X-Ray Scattering and Grazing-Incidence Small-Angle X-Ray Scattering," *Journal of Applied Crystallography* 47 (2014): 1797–1803.

33. A. Buffet, A. Rothkirch, R. Döhrmann, et al., "P03, the Microfocus and Nanofocus X-Ray Scattering (MiNaXS) Beamline of the PETRA III Storage Ring: The Microfocus Endstation," *Journal of Synchrotron Radiation* 19, no. 4 (2012): 647–653.

34. P. Zhang, G. Santoro, S. Yu, S. K. Vayalil, S. Bommel, and S. V. Roth, "Manipulating the Assembly of Spray-Deposited Nanocolloids: In Situ Study and Monolayer Film Preparation," *Langmuir* 32 (2016): 4251–4258.

35. C. J. Schaffer, C. M. Palumbiny, M. A. Niedermeier, et al., "A Direct Evidence of Morphological Degradation on a Nanometer Scale in Polymer Solar Cells," *Advanced Materials* 25 (2013): 6760–6764.

36. W. Quevedo, M. Petri, G. Busse, and S. Techert, "On the Mechanism of Photoinduced Phase Transitions in Ternary Liquid Crystal Systems Near Thermal Equilibrium," *The Journal of Chemical Physics* 129 (2008): 024502.

37. W. Quevedo, G. Busse, J. Hallmann, et al., "Ultrafast Time Dynamics Studies of Periodic Lattices With Free Electron Laser Radiation," *Journal of Applied Physics* 112 (2012): 093519.

38. M. Doucet, H. Cho Jae, G. Alina, et al., "SasView Version 503," (2020), https://doi.org/10.5281/zenodo.3930098.

39. H. Yang, S. Yang, J. Kong, A. Dong, and S. Yu, "Obtaining Information About Protein Secondary Structures in Aqueous Solution Using Fourier Transform IR Spectroscopy," *Nature Protocols* 10 (2015): 382–396.

40. P. Ruelle and U. W. Kesselring, "The Hydrophobic Effect. 3. A Key Ingredient in Predicting n-Octanol–Water Partition Coefficients," *Journal of Pharmaceutical Sciences* 87, no. 8 (1998): 1015–1024.

41. R. A. Pierotti, "A Scaled Particle Theory of Aqueous and Nonaqueous Solutions," *Chemical Reviews* 76 (1976): 717–726.

42. J. C. Dearden and G. M. Bresnen, "Thermodynamics of Water-Octanol and Water-Cyclohexane Partitioning of some Aromatic Compounds," *International Journal of Molecular Sciences* 6 (2005): 119–129.

43. Cambridge MedChem Consulting CC BY 30 2019 https://pubchem.ncbi.nlm.nih.gov/bioassay/19424.

44. K. T. Savjani, A. K. Gajjar, and J. K. Savjani, "Drug Solubility: Importance and Enhancement Techniques," *ISRN Pharmaceutics* 2012 (2012): 195727.

45. M. C. Wenlock, R. P. Austin, P. Barton, A. M. Davis, and P. D. Leeson, "A Comparison of Physiochemical Property Profiles of Development and



2365709x, 2026, 20, Downloaded from https://advanced.onlinelibrary.wiley.com/doi/10.1002/admt.71285 by DESY - Zentralbibliothek, Wiley Online Library on [03/11/2026]. See the Terms and Conditions (https://onlinelibrary.wiley.com/terms-and-conditions) on Wiley Online Library for rules of use; OA articles are governed by the applicable Creative Commons License

Marketed Oral Drugs," *Journal of Medicinal Chemistry* 46 (2003): 1250–1256.

46. J. A. Arnot and S. L. Planey, "The Influence of Lipophilicity in Drug Discovery and Design," *Expert Opinion on Drug Discovery* 7, no. 10 (2012): 863–875.

47. M. J. Waring, "Lipophilicity in Drug Discovery," *Expert Opinion on Drug Discovery* 5, no. 3 (2010): 235–248.

48. S. Lobo, "Is There Enough Focus on Lipophilicity in Drug Discovery?," *Expert Opinion on Drug Discovery* 15, no. 3 (2020): 261–263.

## Supporting Information

Additional supporting information can be found online in the Supporting Information section.

**Supporting File**: admt71285-sup-0001-SuppMat.docx.



2365709x, 2026, 20, Downloaded from https://advanced.onlinelibrary.wiley.com/doi/10.1002/admt.71285 by DESY - Zentralbibliothek, Wiley Online Library on [03/11/2026]. See the Terms and Conditions (https://onlinelibrary.wiley.com/terms-and-conditions) on Wiley Online Library for rules of use; OA articles are governed by the applicable Creative Commons License